

1 **Experimental assessment of the relationship between**
2 **rainfall intensity and sinkholes caused by damaged sewer**
3 **pipes**

4
5 Tae-Young Kwak¹, Sang-Inn Woo², Choong-Ki Chung³, and Joonyoung Kim⁴

6 ¹Seismic Safety Research Center, Korea Institute of Civil Engineering and Building Technology, Goyang-si,
7 Gyeonggi-do 10223, South Korea.

8 ²Department of Architectural & Civil Engineering, Hannam University, Daedeok-gu, Daejeon 34430, South
9 Korea.

10 ³Department of Civil & Environmental Engineering, Seoul National University, Gwanak-gu, Seoul 08826,
11 South Korea.

12 ⁴Division of Smart Interdisciplinary Engineering, Hannam University, Daedeok-gu, Daejeon 34430, South
13 Korea.

14 *Correspondence to:* Joonyoung Kim (goldenrain91@gmail.com)

15 **ABSTRACT**

16 In several countries, the rising occurrence of sinkholes has led to severe social and economic damage. Based
17 on the mechanism of sinkhole development, researchers have investigated the correlation between rainfall
18 intensity and sinkholes caused by damaged sewer pipes. In this study, the effect of rainfall intensity on the
19 formation of eroded zones, as well as the occurrence of sinkholes caused by soil erosion due to groundwater
20 infiltration through pipe defects, has been analyzed through model tests. The ground in Seoul was adopted
21 using weathered granite soil, which is generally used for backfill sewer pipes, and groundwater levels
22 corresponding to three different rainfall intensity conditions were considered. The ground level changes and
23 ground displacements were measured continuously, and the particle image velocimetry (PIV) algorithm was
24 applied to measure the displacement at each position of the model ground. The results indicate that impeding
25 the excessive rise of groundwater levels by securing sufficient sewage treatment facilities can effectively
26 prevent the development of sinkholes caused by pipe defects.

27
28
29



30 1 Introduction

31 In recent times, cases of sinkholes (or **ground cave-ins**) have been reported in several countries, such as the
32 US, Japan, Italy, South Africa, China, and South Korea. Major social and economic issues have ensued owing
33 to the resulting structural problems, such as the collapse of buildings and road erosion (Bae et al., 2016;
34 Galloway et al., 1999; Gao et al., 2013; Guarino and Nisio, 2012; Intrieri et al., 2015; Kuwano et al., 2010a;
35 Oosthuizen and Richardson, 2011; Yokota et al., 2012). In general, sinkholes can be classified into two types:
36 (1) natural sinkholes and (2) anthropogenic sinkholes. Natural sinkholes occur when the underlying ground
37 layer (e.g., karst landscape) is easily soluble in water, whereas anthropogenic sinkholes occur in a non-karst
38 environment, caused by human activity such as sewage damage, inadvertent excavation, or groundwater
39 lowering.

40 Both types of sinkholes have similar mechanisms, and the detailed process of occurrence is as follows
41 (Brinkmann et al., 2008; Caramanna et al., 2008; Kuwano et al., 2010a; Martinotti et al., 2017; Oosthuizen
42 and Richardson, 2011; Rogers, 1986): (1) A cavity is formed underground by external factors (the water-
43 soluble ground layer dissolves in groundwater to cause a natural sinkhole, or soil erosion occurs along with
44 the groundwater outflow due to sewage damage or excavation to cause an anthropogenic sinkhole). (2) The
45 groundwater level rises during rainfall and falls after the rainfall, causing the soil around the cavity to be lost
46 and the cavity to expand. (3) A sinkhole is finally generated because of the repeated increase and decrease of
47 the groundwater level.

48 Based on the mechanism for both types of sinkholes (natural and anthropogenic), a direct relationship can be
49 inferred between the rainfall intensity, which leads to the transition of the groundwater level (rise and fall),
50 and the occurrence of sinkhole. Notably, the change in climate due to global warming has resulted in higher
51 rainfall intensity with fewer rainy days (Alpert et al., 2002; Kristo et al., 2017; Rahardjo et al., 2019a, 2019b).
52 In South Korea, the maximum daily rainfall has increased over the decades in most regions and is expected
53 to increase significantly in the future (Choi et al., 2017; Nadarajah and Choi, 2007; Wi et al., 2016). Thus,
54 there is a growing need to study the correlation between rainfall intensity and sinkhole occurrence.

55 Martinotti et al. (2017) showed that a period of torrential rain and the rainfall intensity triggered the natural
56 sinkholes in Italy. Gao et al. (2013) confirmed that the groundwater level rise due to extremely heavy rainfall
57 has a significant effect on sinkhole generation in a karst environment in China. Van Den Eeckhaut et al.
58 (2007) showed that the formation of numerous natural sinkholes in Belgium corresponded with periods of
59 high rainfall and high groundwater recharge, which commonly increased the weight of the overburden and
60 decreased its cohesion.

61 The majority of sinkholes in non-karst environments are known to occur because of damaged sewer pipes.
62 In Seoul, South Korea, an average of 677 sinkholes and subsidence occurred annually from 2010 to 2015, of
63 which 81.4 % were due to damage to old sewer pipes (Bae et al., 2016). In Japan, local governments in
64 sewage projects were surveyed to identify cases of subsidence due to damage to sewer pipes. As a result, a
65 total of 17,000 data were reported from 2006 to 2009 (Yokota et al., 2012).

66 Considering these factors, several researchers have conducted statistical analysis and model experiments to
67 investigate the correlation between rainfall intensity and sinkholes caused by damaged sewer pipes. Kwak et
68 al. (2016) showed that the number of anthropogenic ~~ground cave-in cases~~ increased with the increase in total
69 monthly precipitation. In addition, it was confirmed that ~~ground cave-ins~~ are prone to occur after
70 exceptionally heavy rains. By quantifying Pearson's correlation coefficient between two relevant
71 observations, Choi et al. (2017) showed that the monthly accumulated precipitation and the quantity of
72 subsidence are related to a certain extent. Guo et al. (2013) and Tang et al. (2017) used model experiments
73 and evaluated the effect of the defect size, groundwater level, and particle size on soil erosion due to
74 groundwater infiltration through pipe defects. However, they only used non-cohesive soils and covered
75 extreme cases with groundwater levels significantly exceeding the ground level.

76 In this study, the urban area in Seoul has been simulated, and model tests have been conducted to analyze the
77 effect of rainfall intensity on the formation of eroded zones, as well as the occurrence of sinkholes caused by
78 soil erosion due to groundwater infiltration through pipe defects. The model ground was constructed using
79 weathered granite soil (which is generally cohesive), ~~which is~~ mainly used to backfill the sewer pipes in
80 Seoul. Three rainfall intensity conditions (heavy rainfall, very heavy rainfall, and extremely heavy rainfall)
81 were set for the groundwater level, based on summer rainfall patterns in Korea, to be applied in the model
82 tests. The groundwater level change, discharged soil volume, and ground displacement were measured
83 continuously throughout the tests. In particular, the particle image velocimetry (PIV) method, which can
84 continuously measure and analyze the displacements in the ground, was applied to quantify the ground
85 deformation with the occurrence and expansion of underground cavities.

86 The remainder of this paper is organized as follows. ~~Sect. 2~~ describes the model test device, model grounds,
87 and test conditions. ~~Sect. 3~~ discusses the model test results. Finally, ~~Sect. 4~~ presents the conclusions ~~and~~
88 ~~contributions of this paper.~~

89 **2 Experimental program**

90 **2.1 Experiment apparatus**

91 In this study, experiments were performed using the model tester developed by Kwak et al. (2019) to simulate
92 ground subsidence (Figure 1). The distance between each pipe in the sewer pipe network in Seoul was
93 examined and found to be around 1.2 m. In order to exclude the effects of unnecessary boundary conditions,
94 the width of the model soil was set to 1.4 m, with respective left and right margins of 0.1 m. Considering that
95 the average landfill depth of a sewage pipe in Seoul is 0.9 m (Kim et al., 2018), the soil chamber was built to
96 a height of 1.0 m, including a 0.1 m clearance to facilitate sample composition. The depth of the soil chamber
97 was set to 0.1 m to simulate the plane strain condition, and the front plate of the chamber was made of acrylic
98 plate to allow the inside of the ground to be photographed during the test.

99

100 A slit was installed at the bottom of the soil chamber to simulate the damage of the sewer pipe allowing the
101 inflow and outflow of sewage and the outflow of soil during the model test. The width of the slit was set to
102 2 cm, based on the study by Mukunoki et al. (2012), such that B/D_{max} was 4.2 (the maximum particle diameter
103 of weathered soil $D_{max} = 4.76$ mm). A supply valve and a drain valve were installed under the slit to control
104 the inflow and outflow of groundwater as well as the outflow of eroded soil. The external water tank
105 connected to the inlet valve was designed to maintain a constant level even when water is continuously
106 supplied to the model ground. Through experimental assessment (Table 1), the National Disaster Management
107 Institute of Korea (2014) suggested a relationship between the rainfall intensity and the hydraulic head in the
108 sewage network conditions near Gangnam station. It should be noted that the hydraulic head increases
109 linearly with the rainfall strength until the rainfall strength is 40 mm/h, but thereafter increases sharply. In
110 the present study, the height of the external tank was made adjustable to simulate the various rainfall intensity
111 (related to hydraulic head).

112 2.2 Model ground

113 The vast majority of prior studies that have experimentally assessed the ground subsidence and sinkhole due
114 to sewer pipe damage have been conducted on poorly-graded non-cohesive soils (Guo et al., 2013; Indiketiya
115 et al., 2017; Kuwano et al., 2010a, 2010b; Sato and Kuwano, 2015; Tang et al., 2017). However, in several
116 countries, the sewage reclamation specifications allow the landfill soil to contain 15–25 % of fine contents.
117 There are no restrictions on particle size distribution apart from the maximum particle size and #No. 4 sieve
118 passing (Japan Road Association, 1990; Ministry of Environment of Korea, 2010). In the present study, to
119 simulate the ground in Seoul in which weathered granite soil, which is a well-graded cohesive soil, is widely
120 distributed, the model ground was created by collecting Gwanak weathered soil and adjusting the fine content
121 to 7.5% to meet the fine content standard. The degree of compaction was also set to 93 % of the standard
122 maximum unit dry weight $\gamma_{d,max}$ to satisfy the sewer pipe landfill standards, and the model ground was
123 constructed with the optimum moisture content. Figure 2 shows the particle size distributions of the adjusted
124 and natural Gwanak soil in comparison with the sewer pipe landfill standards in South Korea and Japan.
125 Table 2 lists the basic physical properties, strength parameters and saturated permeability coefficient of the
126 adjusted Gwanak soil used in the model test.

127 2.3 Digital image analysis

128 In geotechnical engineering, digital imaging techniques are primarily used to measure the deformation of
129 target samples (Alshibli and Sture, 1999; Indiketiya et al., 2017; Kim et al., 2017; Kwak et al., 2019; White
130 et al., 2003). In the present study, the displacement at each position of the model ground was measured by
131 applying the PIV algorithm (Adrian, 1991), which is the most widely used technique in the field of
132 geotechnical engineering. The PIV cross-correlation on the pixel sets of the pre-deformation and post-
133 deformation images were calculated to obtain the point with the highest correlation. The position of the

134 sample set with the highest correlation is used to estimate the relative displacement at each position of the
135 sample (Kim et al., 2011; White et al., 2003). In this study, the internal displacement of the sample was
136 evaluated using GeoPIV (White and Take, 2002), a commercial program that is widely used to apply the PIV
137 technique in geotechnical engineering. With the displacement, the volume and shear strain are estimated
138 together for the analysis.

139 In general, when applying the PIV technique, high accuracy analysis results can be obtained when the
140 uniqueness of the pixel set increases as the size of the pixel set increases. However, in order to calculate
141 displacements at various positions, it is necessary to set an appropriate size for the set of pixels. Accuracy
142 and precision verification of the GeoPIV program was performed for this, and the size of the pixel set was
143 set to 100 by 100 pixels as a result. As shown in Figure 3, the PIV technique was applied to the positions of
144 a total of 2600 pixel subsets (65 by 40). To minimize the boundary effect between the interface of the sample
145 and the soil chamber, the vicinity of the wall was excluded from the analysis. In addition, any excessive
146 relative displacement due to soil erosion (no highly correlated pixel sets found in the post-deformation image)
147 was excluded from the analysis.

148 **2.4 Test procedures**

149 Once the model ground was created, the model tests which consisted of multiple cycles were conducted.
150 Each experimental cycle consisted of a water supply stage that simulated the rainfall and a water drainage
151 stage that simulated the aftereffect of the rainfall. During the water supply stage, water from the external
152 ~~water~~ tank was introduced into the soil chamber through the supply valve to reach the target groundwater
153 level. Following this, during the water drainage stage, the supply valve was closed and the drainage valve
154 ~~was~~ opened to allow the soil to discharge through the lower slit along with the water. Table 3 shows the
155 conditions of the three model tests conducted in this study, simulating cases with rainfall intensities of 40
156 mm/h and 50 mm/h presented in Table 1, as well as that with the groundwater level rising to the ground
157 surface.

158 Linear variable displacement transducers (LVDTs) were installed at three locations on the surface of the
159 ground, at 0, 30, and 60 cm from the center of the soil chamber, to measure the surface displacement during
160 the tests (Figure 1). During the model tests, digital images of the ground were continuously captured, and the
161 PIV technique was applied to analyze the displacement and deformation (Adrian, 1991; Alshibli and Akbas,
162 2007; Kim et al., 2017; Kwak et al., 2019). In addition, the amount of soil discharged through the slit was
163 measured after the water supply and water drainage stages of each test.

164 **3 Experimental results and discussion**

165 **3.1 Test 1: Heavy rainfall intensity (47 cm hydraulic head)**

166 **3.1.1 Water supply stage**

167 Test 1 was conducted by introducing groundwater to a 47 cm initial hydraulic head (the height difference
168 between the slit and weir in the water tank) to simulate a heavy rainfall intensity of 40 mm/h. In the water
169 supply stage of Test 1, no soil deformation occurred on the ground surface (measured by the LVDTs) and in
170 the ground (measured by the PIV technique) as the groundwater level approached 47 cm. Immediately after
171 opening the slit, the water pressure acting on the ground directly above the slit was 4.5 kPa, and the vertical
172 earth pressure generated by the upper soil was about 16.7 kPa. Therefore, under this condition, the soil always
173 had a positive effective stress, and the piping phenomenon did not occur. In this study, since the model ground
174 was densely constructed ($D_R = 78\%$) with a sufficient degree of compaction ($R_C = 93\%$) according to
175 domestic specification, no water compaction (Kwak et al., 2019), which occurs mainly when sewage flows
176 into a loose sandy soil, was observed. From these results, it was confirmed in this experimental case that the
177 resistance factor (due to the soil strength parameter) was greater than the sum of the drag force (upward force
178 by infiltration pressure during water supply) and the gravity (downward force).

179 **3.1.2 Water drainage stage**

180 In the water drainage stage of Test 1, no soil deformation was observed on the ground surface as in the water
181 supply stage. The deformation in the ground was evaluated by applying PIV to the images captured during
182 the test. Figures 4, 5, 6 are the PIV analysis results showing the estimated displacement vector, volume, and
183 shear strain increments in six phases: (a) 0–30 s, (b) 30–60 s, (c) 60–90 s, (d) 90–120 s, (e) 120–150 s, and
184 (f) 150–180 s. For the volumetric strain, the red grid (the area with positive values) indicates that the area has
185 expanded, and the blue grid (the area with negative values) indicates that the area has been compressed.

186 In the water drainage stage, the water pressure applied through the slit disappeared, and the groundwater in
187 the soil chamber was discharged quickly through the slit. Unlike in the water supply stage, the ground below
188 the groundwater level became saturated and lost its apparent cohesion. The rapid outflow of groundwater
189 resulted in a downward infiltration into the ground, and the soil was discharged from the area immediately
190 above the slit, where there was no active restraining pressure (and thus, no shear strength), along with the
191 groundwater.

192 During the initial phase of the water drainage stage (0–60 s), the soil was discharged through the slit, causing
193 a downward displacement in the periphery of the cavity, and a triangular cavity was formed just above the
194 slit (Figure 4 (a) and (b)). In addition, volume and shear strain increments occurred intensively around the
195 cavity (Figure 5 (a), (b), Figure 6 (a) and (b)). In the 60–90 s interval of the water drainage stage, as shown
196 in Figure 4 (c), the soils on the both sides of the cavity collapsed, and the cavity expanded laterally. The

197 volume and shear strain increments were concentrated in small areas near the cavity, similar to the initial
198 stage (Figure 5 (c) and Figure 6 (c)).

199 As shown in Figure 4 (d), during the 90–120 s interval of the groundwater drainage stage, the lateral
200 expansion of the cavity inside the ground was completed, and no downward displacement was observed in
201 the upper part of the cavity and the soils on the sides. The volume and shear strain increments were also not
202 observed in the outer region of the cavity (Figure 5 (d) and Figure 6 (d)). In this phase, the cavity collapsed;
203 the soil accumulated near the slit gradually shifted to escape into the slit, and the deformation was
204 concentrated near the slit. After 120 s, the soil regained its apparent adhesion due to surface tension, and its
205 outflow stabilized as the drainage completed. Finally, a mushroom-shaped cavity was formed (Figure 4 (e)
206 and (f)).

207 **3.2 Test 2: Very heavy rainfall intensity (70 cm hydraulic head)**

208 **3.2.1 Water supply stage**

209 Test 2 was conducted by setting the maximum groundwater level to 70 cm to simulate a high rainfall intensity
210 of 50 mm/h. During the water supply stage of Test 2, no soil deformation was observed on the ground surface
211 and in the ground by both LVDT and PIV analyses. As a result, owing to the soil strength parameter, the
212 resistance factor was found to remain greater than the sum of the drag force (upward force by infiltration
213 pressure during water supply) and the gravity (downward force), despite the application of a higher hydraulic
214 pressure in Test 2 as compared to that in Test 1.

215 **3.2.2 Water drainage stage**

216 During the water drainage stage of Test 2, no vertical displacement was observed on the surface of the model
217 ground. The displacement of the soil element according to the development of the underground cavity was
218 observed by the PIV technique. Figures 7, 8, and 9 show the displacement increment vectors, incremental
219 volumetric strain distribution, and incremental shear strain distribution, respectively; the analysis was
220 conducted in four phases: 0–30 s, (b) 30–60 s, (c) 60–90 s, and (d) 90–120 s (the displacement ended within
221 120 s).

222 In the initial phase of the water drainage stage (0–30 s), the soil was discharged through the slit, causing an
223 internal collapse near the slit. Thus, an underground cavity was formed (Figure 7 (a)), differing from that in
224 Test 1 in terms of shape as well as location; it was located close to the maximum groundwater level (about
225 60 cm from the bottom plate). These results indicate that the hydraulic pressure (related to rainfall intensity)
226 affects the shape and location of the underground cavity in the water drainage stage. In Test 1, the eroded
227 zone was formed up to about 89 % of the maximum groundwater level. In Test 2, it developed up to about
228 86 %. When a poorly-graded non-cohesive soil was used under the same experimental conditions, the cavity
229 developed up to 107 % of the maximum groundwater level (Kwak et al., 2019). This shows that the well-
230 graded cohesive soil used in this study has a greater resistance to soil erosion. In addition, during the initial

231 stage (0–30 s), the incremental volumetric and shear strains were found to be concentrated in the upper area
232 of the underground cavity (Figure 8 (a) and Figure 9 (a)).
233 During the 30–90 s phase, downward displacement was no longer observed at the top of the cavity;
234 displacement in the slit direction occurred only in the left and right areas adjacent to the cavity (Figure 7 (b)
235 and (c)). The volumetric and shear strains also showed a tendency to be concentrated in the left and right
236 areas where the displacement occurred, indicating that the cavity gradually increased laterally (Figure 8 (b),
237 (c), Figure 9 (b), and (c)). In the process of forming a cavity, the downward infiltration pressure was low,
238 and the soil that had lost strength accumulated near the slit. On the other hand, when the downward infiltration
239 pressure was higher, all the soil that had lost strength escaped, resulting in the formation of an oval cavity.
240 After 90 s, as the groundwater level was exhausted, the unsaturated strength of the ground was restored, and
241 no further displacement or deformation were observed inside the ground (Figure 7 (d), Figure 8 (d), and
242 Figure 9 (d)).

243 **3.3 Test 3: Extremely heavy rainfall intensity (90 cm hydraulic head)**

244 **3.3.1 Water supply stage**

245 Test 3 was conducted to simulate the intensity of an extremely heavy rainfall that causes the groundwater
246 level to rise up to the surface of the ground. In the water supply stage of Test 3, significant displacements
247 were measured on the surface (LVDTs) and inside the model ground (PIV). Figure 10 shows the surface
248 displacement over time, with a gradual subsidence after approximately 2400 s. The ground displacements
249 identified by the PIV technique from 0–2000 s also showed no specific behaviors. Therefore, the internal
250 displacement vectors identified as a result of the PIV technique after 2000 s are shown in Figure 11, overlaid
251 onto the final photograph of each step: (a) 2000–2400 s, (b) 2400–2800 s, (c) 2800–3200 s, and (d) 3200–
252 3600 s.

253 As the groundwater level reached about 75 cm (83 % of ground height), soil particle displacement was
254 observed in the soil from 2000–2400 s. This result indicates that, owing to the strength of the soil, the
255 resistance factor becomes smaller as the model ground is saturated, and the weight of the soil in the saturated
256 region cannot be supported. Since the soil in the upper part of the groundwater level still maintained its
257 unsaturated strength, the downward displacement appeared only in the area adjacent to the groundwater level.
258 There was still no subsidence observed on the surface (Figure 11 (a)).

259 From 2400–2800 s, downward displacement towards the slit was observed throughout the soil area. In
260 particular, a larger downward displacement was observed in the inverted triangle region above the slit, which
261 was significantly affected by the inflow of groundwater (Figure 11 (b)). As the groundwater level rose, the
262 matric suction expressed in the unsaturated region of the ground decreased. Therefore, the subsidence on the
263 ground surface was also measured from this phase. From 2800–3200 s, the groundwater level reached 80 cm
264 from the bottom (89 % of ground height), and the maximum downward displacement of the entire water
265 supply stage was observed during this phase (Figure 11 (c)). This indicates that infiltration occurs when the

266 groundwater level approaches the ground surface, and the soil structure is no longer supported as there is no
267 longer sufficient matric suction in the ground directly above the groundwater level. After 3200 s, downward
268 displacement occurred continuously throughout the soil area until groundwater level reaches the target level
269 (Figure 11(d)).

270 **3.3.2 Water drainage stage**

271 The water drainage stage of Test 3 was divided into four phases for the analysis: (a) 0–30 s, (b) 30–60 s, (c)
272 60–90 s, and (d) 90–120 s. The displacement increment vectors, incremental volumetric strain distributions,
273 and incremental shear strain distributions of each stage are shown in Figure 12, 13 and 14, respectively,
274 overlaid onto the photograph of the target ground taken at the end of each phase.

275 In the initial phase (0–30 s) of the water drainage stage of Test 3, the groundwater was rapidly discharged
276 into the slit owing to high downward infiltration pressure. As the soil particles escaped along with the
277 groundwater discharge, the upper ground collapsed, forming an anthropogenic sinkhole similar in shape to
278 the punching shear failure (Figure 12(a)). In the previous tests, the cavities formed up to about 86 % and
279 89 % of the maximum groundwater level. However, in this case, the upper soil layer became inordinately
280 thin and eventually collapsed inwards. The shape of the formed anthropogenic sinkhole indicated significant
281 downward displacement (of the soil that had lost strength) towards the slit. The sudden collapse of the ground
282 clogged the slit, which in turn prevented soil discharge. At this time, the shear deformation also showed a
283 tendency to be concentrated around the collapsed soil (Figure 14(a)). After the soil was completely drained,
284 no significant deformation inside the ground and on the ground surface were observed via the PIV technique
285 and the LVDTs after 30 s, as the matric suction allowed the ground to recover its unsaturated strength.

286 **3.4 Comparative Study**

287 To quantitatively analyze the effect of rainfall intensity on ground cavity and sinkhole development, the
288 evolution of the cavity size with time in the water drainage stage was obtained for each test, and the time at
289 which the water was completely drained was also displayed, as shown in Figure 15. For the hydraulic pressure
290 of 45 cm and 70 cm, the time taken for the groundwater to drain completely was 70 s and 90 s, respectively.
291 However, in Test 3, although the groundwater level was higher, the soil collapsed instantly, resulting in an
292 anthropogenic sinkhole, and the time taken for complete drainage was 80 s, which was faster than that in Test
293 2. After the drainage was completed, the cavity sizes measured in Test 1 and Test 2 were 497 cm² (66 % of
294 the final cavity size of 742 cm²) and 1286 cm² (87 % of the final cavity size of 1482 cm²), respectively. In
295 both Tests 1 and 2, the cavity expanded for about 30 s after the drainage was completed, at which time its
296 size tended to stabilize. In Test 3, where the anthropogenic sinkhole occurred, a cavity of 1207 cm² (56 % of
297 the final cavity size of 2171 cm²) was formed after the drainage was completed, after which the cavity
298 continued to expand for approximately 200 s.

299 Table 4 shows the ratio of the weight of the total soil volume to the weight of the discharged soil volume, the
300 volume ratio of the area corresponding to the cavity, and the weight ratio of the loosening zone, respectively.
301 The size and internal density change of the loosening zone were calculated by the following method. (1)
302 After completion of the test, the discharged soil was dried to measure the weight. (2) The weight of the area
303 corresponding to the cavity was calculated by multiplying the calculated volume of the cavity by the initial
304 density of the soil. The soil weight corresponding to the loosening zone was calculated through the difference
305 between the results of steps (1) and (2). (3) The size of the loosening zone was calculated by excluding the
306 area corresponding to the cavity from the area overlapping with the volumetric strain calculated in each step.
307 (4) The internal density change was confirmed using the results of steps (2) and (3).
308 As shown in Table 4, the size and density change of the loosening area were found to be nearly identical in
309 the three tests. On the other hand, as the hydraulic head increased, the weight and volume of the eroded zone
310 and the average width of the cavity relative to the slit width increased linearly. However, recalling the fact
311 that the hydraulic head increased drastically when the rainfall intensity exceeds a certain threshold, it can be
312 inferred that the volume of the discharged soil and the size of the eroded zone may also increase exponentially
313 with rainfall intensity. The threshold value is definitely specific to a given sewer-system. Thus the
314 experimental results of this study suggest that to prevent sinkholes caused by pipe defects, sewage pipe
315 network facilities need to be expanded to inhibit the rapid rise of groundwater levels in preparation for
316 increased torrential rain caused by climate change.

317 **4 Conclusions**

318 In this study, model tests were used to analyze the effects of rainfall intensity on the formation of the eroded
319 zone and the occurrence of sinkholes caused by soil erosions due to groundwater infiltration through pipe
320 defects. The model tests were conducted to simulate the actual site conditions as far as possible by using the
321 soil used around sewer pipe networks and the sewer pipe landfill standards as well as a large-scale soil
322 chamber. The groundwater level was applied to the model tests by setting three hydraulic heads based on the
323 heavy rainfall characteristics of South Korea: (1) heavy rainfall intensity (47 cm hydraulic head); (2) very
324 heavy rainfall intensity (70 cm hydraulic head); and (3) extremely heavy rainfall intensity (90 cm hydraulic
325 head). Throughout the model tests, the groundwater level changes and the ground surface displacements were
326 measured continuously from the start to the end of the tests. In addition, the PIV technique, which can
327 continuously measure and analyze the displacement of the entire ground, was applied to quantify the ground
328 deformation (volumetric strain and shear strain), generation, and expansion of the underground cavity. Based
329 on the results of the three tests, the following observations were drawn:

- 330 (1) The rainfall intensity considerably affected on the ground deformation during and after a rainfall.
- 331 (2) Under heavy and very heavy rainfall intensity conditions, no internal soil deformation occurred while the
332 groundwater level was rising. However, under extremely heavy rainfall intensity conditions, ground
333 subsidence was observed. This result indicates that the resistance factor (due to the soil strength parameter)

334 becomes smaller than the sum of the drag force (upward force by infiltration pressure during water supply)
335 and the gravity (downward force) when the rainfall intensity exceeds a certain threshold, which was found
336 to have a hydraulic head between 70 cm and 90 cm under the given system.

337 (3) After heavy rainfall (that leads to the rise of the groundwater level due to the infiltration of groundwater
338 through the sewer pipe defects), the soil was discharged from the area above the slit with the rapid outflow
339 of groundwater, where there was no active restraining pressure. During the formation and development of
340 cavity along with the drop in the groundwater level, the incremental volumetric and shear strains were
341 concentrated in the vicinity of the underground cavity.

342 (4) The height and average width of cavities increased linearly with the applied hydraulic head, and notably,
343 sinkhole opened under extremely heavy rainfall intensity. Referring the previous study which showed the
344 relationship between the hydraulic head and rainfall intensity, the discharged soil and the size of the eroded
345 zone may increase exponentially with rainfall intensity.

346 It should be noted that the hydraulic head-rainfall intensity relationship used in this study is site-specific. The
347 induced hydraulic head under the same rainfall intensity can be different site to site. Nevertheless, the
348 experimental observations of this study confirm the influence of rainfall intensity on the soil erosion near the
349 sewer pipe defects as well as sinkhole occurrence and suggest a necessity of sewage pipe network facilities
350 rehabilitation in preparation for increased torrential rain caused by climate change.

351 **Author contribution**

352 The conceptualization was done by TYK, CKC, and JK planned methodology. TYK performed the analysis
353 using software, and validation was performed by SIW and CKC. JK performed formal analysis. TYK
354 prepared the original draft, while all authors contributed to the review and editing. Visualization and graphics
355 were designed by TYK and JK. SIW and CKC supervised the research work.

356 **Competing interests**

357 The authors declare that they have no conflict of interest



358 **Acknowledgements**

359 This research was supported by the Research Institute at the college of Engineering of Seoul National
360 University. In addition, the support of Jin-Tae Han, research fellow of the Korea Institute of Civil Engineering
361 & Building Technology, is greatly appreciated.

362 **Financial support**


363 This research was supported by a grant (code: 20SCIP-C151438-02) from Construction Technologies
364 Program funded by Ministry of Land, Infrastructure and Transport of Korean government. Also, this work
365 was supported by the National Research Foundation of Korea (NRF) grant funded by the South Korean
366 government (MSIP) (No. 2015R1A2A1A01007980).

367 **References**

- 368 Adrian, R. J.: Particle-Imaging Techniques for Experimental Fluid Mechanics, *Annu. Rev. Fluid Mech.*,
369 23(1), 261–304, doi:10.1146/annurev.fl.23.010191.001401, 1991.
- 370 Alpert, P., Ben-Gai, T., Baharad, A., Benjamini, Y., Yekutieli, D., Colacino, M., Diodato, L., Ramis, C.,
371 Homar, V., Romero, R., Michaelides, S. and Manes, A.: The paradoxical increase of Mediterranean
372 extreme daily rainfall in spite of decrease in total values, *Geophys. Res. Lett.*, 29(11), 29–32,
373 doi:10.1029/2001GL013554, 2002.
- 374 Alshibli, K. A. and Akbas, I. S.: Strain Localization in Clay: Plane Strain versus Triaxial Loading
375 Conditions, *Geotech. Geol. Eng.*, 25(1), 45–55, doi:10.1007/s10706-006-0005-4, 2007.
- 376 Alshibli, K. A. and Sture, S.: Sand Shear Band Thickness Measurements by Digital Imaging Techniques, *J.*
377 *Comput. Civ. Eng.*, 13(April), 103–109, doi:10.1061/(ASCE)0887-3801(1999)13:2(103), 1999.
- 378 Bae, Y., Shin, S., Won, J. and Lee, D.: *The Road Subsidence Conditions and Safety Improvement Plans in*
379 *Seoul*, Seoul., 2016.
- 380  Brinkmann, R., Parise, M. and Dye, D.: Sinkhole distribution in a rapidly developing urban environment:
381 Hillsborough County, Tampa Bay area, Florida, *Eng. Geol.*, 99(3–4), 169–184,
382 doi:10.1016/j.enggeo.2007.11.020, 2008.
- 383 Caramanna, G., Ciotoli, G. and Nisio, S.: A Review of Natural Sinkhole Phenomena in Italian Plain Areas,
384 *Nat. Hazards*, 45(2), 145–172, doi:10.1007/s11069-007-9165-7, 2008.
- 385 Choi, C., Kim, J., Kang, J. and Park, Y.: Ground Subsidence Risk Analysis with Intensity and Duration of
386 Rainfall, *Mod. Environ. Sci. Eng.*, 3(03), 162–167, doi:10.15341/mese(2333-2581)/03.03.2017/003, 2017.
- 387 **Van Den Eeckhaut, M., Poesen, J., Dugar, M., Martens, V. and Duchateau, P.: Sinkhole formation above**
388 **underground limestone quarries: A case study in South Limburg (Belgium), *Geomorphology*, 91(1–2), 19–**
389 **37, doi:10.1016/j.geomorph.2007.01.016, 2007.** 
- 390 Galloway, D., Jones, D. R. and Ingebritsen, S. E.: Land Subsidence in the United States, *United States*
391 *Geol. Surv. Circ.* 1182, 177, 1999.
- 392 Gao, Y., Luo, W., Jiang, X., Lei, M. and Dai, J.: Investigations of Large Scale Sinkhole Collapses, Laibin,
393 Guangxi, China, in *National Cave and Karst Research Institute Symposium 2*, pp. 327–331, Carlsbad, New
394 Mexico., 2013.

395 Guarino, P. M. and Nisio, S.: Anthropogenic Sinkholes in the Territory of the City of Naples (Southern
396 Italy), *Phys. Chem. Earth*, 49, 92–102, doi:10.1016/j.pce.2011.10.023, 2012.

397 Guo, S., Shao, Y., Zhang, T., Zhu, D. Z., Asce, M. and Zhang, Y.: Physical Modeling on Sand Erosion
398 around Defective Sewer Pipes under the Influence of Groundwater, , 139(December), 1247–1257,
399 doi:10.1061/(ASCE)HY.1943-7900.0000785., 2013.

400  Indiketiya, S., Jegatheesan, P. and Pathmanathan, R.: Evaluation of Defective Sewer Pipe Induced Internal
401 Erosion and Associated Ground Deformation Using Laboratory Model Test, *Can. Geotech. J.*, 54(8), 1184–
402 1195, doi:https://doi.org/10.1139/cgj-2016-0558, 2017.

403 Intrieri, E., Gigli, G., Nocentini, M., Lombardi, L., Mugnai, F., Fidolini, F. and Casagli, N.: Sinkhole
404 monitoring and early warning: An experimental and successful GB-InSAR application, *Geomorphology*,
405 241, 304–314, doi:10.1016/j.geomorph.2015.04.018, 2015.

406 Japan Road Association: Earth works manual, 1990.

407 Kim, J., Jang, E.-R. and Chung, C.-K.: Evaluation of Accuracy and Optimization of Digital Image Analysis
408 Technique for Measuring Deformation of Soils, *J. Korean Geotech. Soc.*, 27(7), 5–16, 2011.

409 Kim, J., Woo, S. I. and Chung, C.: Assessment of Non-uniform Deformation during Consolidation with
410 Lateral Drainage using Particle Image Velocimetry (PIV), *KSCE J. Civ. Eng.*, doi:10.1007/s12205-017-
411 0707-6, 2017.

412 Kim, K., Kim, J., Kwak, T. Y. and Chung, C. K.: Logistic Regression Model for Sinkhole Susceptibility
413 due to Damaged Sewer Pipes, *Nat. Hazards*, 93(2), 765–785, doi:10.1007/s11069-018-3323-y, 2018.

414 Kristo, C., Rahardjo, H. and Satyanaga, A.: Effect of Variations in Rainfall Intensity on Slope Stability in
415 Singapore, *Int. Soil Water Conserv. Res.*, 5(4), 258–264, doi:10.1016/j.iswcr.2017.07.001, 2017.

416 Kuwano, R., Horii, T., Yamauchi, K. and Kohashi, H.: Formation of Subsurface Cavity and Loosening due
417 to Defected Sewer Pipes, *Japanese Geotech. J.*, 5(2), 349–361, 2010a.

418 Kuwano, R., Sato, M. and Sera, R.: Study on the Detection of Underground Cavity and Ground Loosening
419 for the Prevention of Ground Cave-in Accident, *Japanese Geotech. J.*, 5(2), 349–361, 2010b.

420 Kwak, T., Kim, J., Lee, M. and Chung, C.-K.: Evaluation of the Factors Contributing to the Occurrence of
421 Ground Cave-ins and Subsidence Induced by a Damaged Sewer Pipeline, in *Civil Engineering Conference*
422 *in the Asian Region (CECAR 7)*, Hawaii, USA., 2016.

423 Kwak, T. Y., Woo, S. I., Kim, J. and Chung, C. K.: Model Test Assessment of the Generation of
424 Underground Cavities and Ground Cave-ins by Damaged Sewer Pipes, *Soils Found.*, 59(3), 586–600,
425 doi:10.1016/j.sandf.2018.12.011, 2019.

426 Martinotti, M. E., Pisano, L., Marchesini, I., Rossi, M., Peruccacci, S., Brunetti, M. T., Melillo, M.,
427 Amoruso, G., Loiacono, P., Vennari, C., Vessia, G., Trabace, M., Parise, M. and Guzzetti, F.: Landslides,
428 Floods and Sinkholes in a Karst Environment: The 1-6 September 2014 Gargano event, southern Italy, *Nat.*
429 *Hazards Earth Syst. Sci.*, 17(3), 467–480, doi:10.5194/nhess-17-467-2017, 2017.


430 Ministry of Environment of Korea: Technical Standard for Construction of Sewer Pipes, 2010.

431 Mukunoki, T., Kumano, N. and Otani, J.: Image Analysis of Soil Failure on Defective Underground Pipe
 432 due to Cyclic Water Supply and Drainage using X-ray CT, *Front. Struct. Civ. Eng.*, 6(2), 85–100,
 433 doi:10.1007/s11709-012-0159-5, 2012.

434 Nadarajah, S. and Choi, D.: Maximum Daily Rainfall in South Korea, *J. Earth Syst. Sci.*, 116(4), 311–320,
 435 doi:10.1007/s12040-007-0028-0, 2007.

436 National Disaster Management Institute of Korea: Possibility of Manhole Cap Removal by Heavy Rainfall,
 437 Minist. Secur. Public Adm. Korea Press Releases, 1–6, 2014.

438 Oosthuizen, A. C. and Richardson, S.: Sinkholes and subsidence in South Africa. [online] Available from:
 439 http://www.geohazard.org.za/images/docs/subsection_downloads/Sinkholes.pdf, 2011.

440  Rahardjo, H., Kim, Y. and Satyanaga, A.: Role of Unsaturated Soil Mechanics in Geotechnical
 441 Engineering, *Int. J. Geo-Engineering*, 10(1), 1–23, doi:10.1186/s40703-019-0104-8, 2019a.

442 Rahardjo, H., Nistor, M. M., Gofar, N., Satyanaga, A., Xiaosheng, Q. and Chui Yee, S. I.: Spatial
 443 distribution, variation and trend of five-day antecedent rainfall in Singapore, *Georisk*, 0(0), 1–15,
 444 doi:10.1080/17499518.2019.1639196, 2019b.

445 Rogers, C. J.: Sewer Deterioration Studies: The Background to the Structural Assessment Procedure in the
 446 Sewerage Rehabilitation Manual., 1986.

447 Sato, M. and Kuwano, R.: Influence of Location of Subsurface Structures on Development of Underground
 448 Cavities induced by Internal Erosion, *Soils Found.*, 55(4), 829–840, doi:10.1016/j.sandf.2015.06.014, 2015.

449 Tang, Y., Zhu, D. Z. and Chan, D. H.: Experimental Study on Submerged Sand Erosion through a Slot on a
 450 Defective Pipe, *J. Hydraul. Eng.*, 143(9), 1–14, doi:10.1061/(ASCE)HY.1943-7900.0001326, 2017.

451 White, D. J. and Take, W. A.: GeoPIV: Particle Image Velocimetry (PIV) Software for Use in
 452 Geotechnical Testing, *Cambridge Univ. Eng. Dep. Tech. Rep.*, 322(October), 15, 2002.

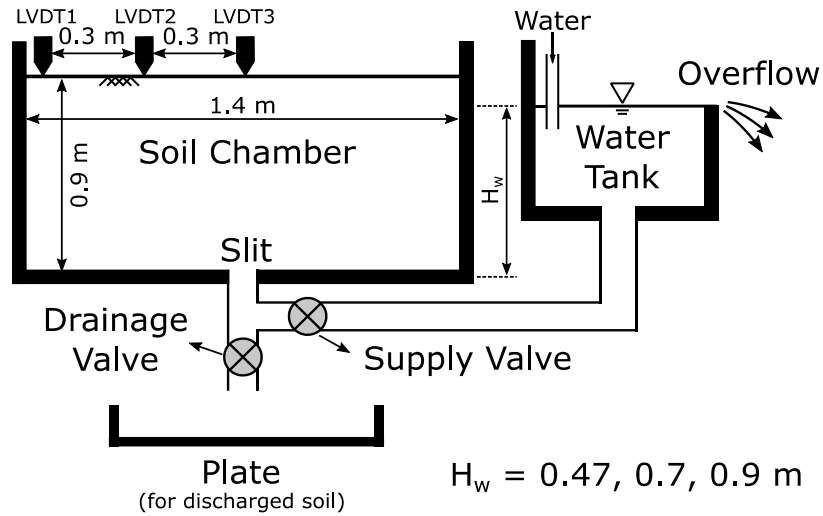
453 White, D. J., Take, W. A. and Bolton, M. D.: Soil Deformation Measurement using Particle Image
 454 Velocimetry (PIV) and Photogrammetry, *Geotechnique*, 53(7), 619–631, doi:10.1680/geot.2003.53.7.619,
 455 2003.

456 Wi, S., Valdés, J. B., Steinschneider, S. and Kim, T. W.: Non-stationary Frequency Analysis of Extreme
 457 Precipitation in South Korea using Peaks-over-threshold and Annual Maxima, *Stoch. Environ. Res. Risk
 458 Assess.*, 30(2), 583–606, doi:10.1007/s00477-015-1180-8, 2016.

459 Yokota, T., Fukatani, W. and Miyamoto, T.: The present situation of the road cave in sinkholes caused by
 460 sewer systems., 2012.

461

462

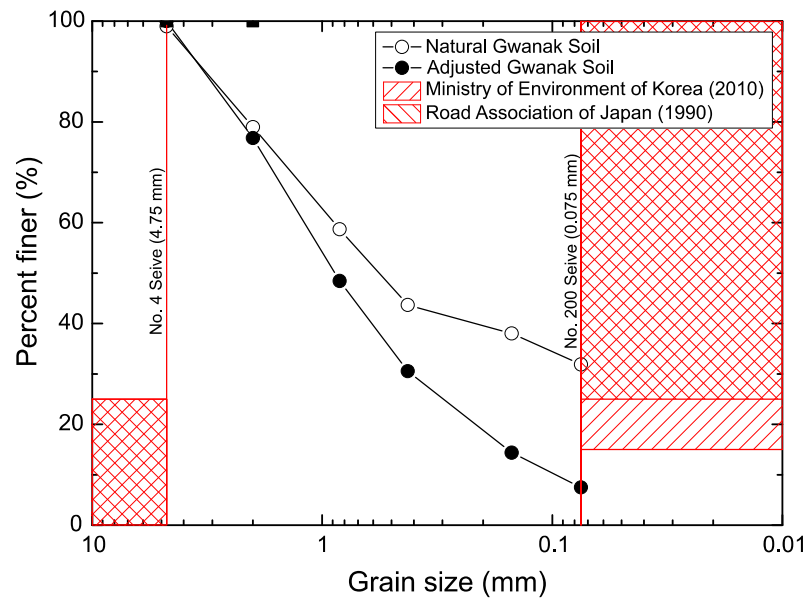


463

464

Figure 1: Schematic of the model test device.

465



466

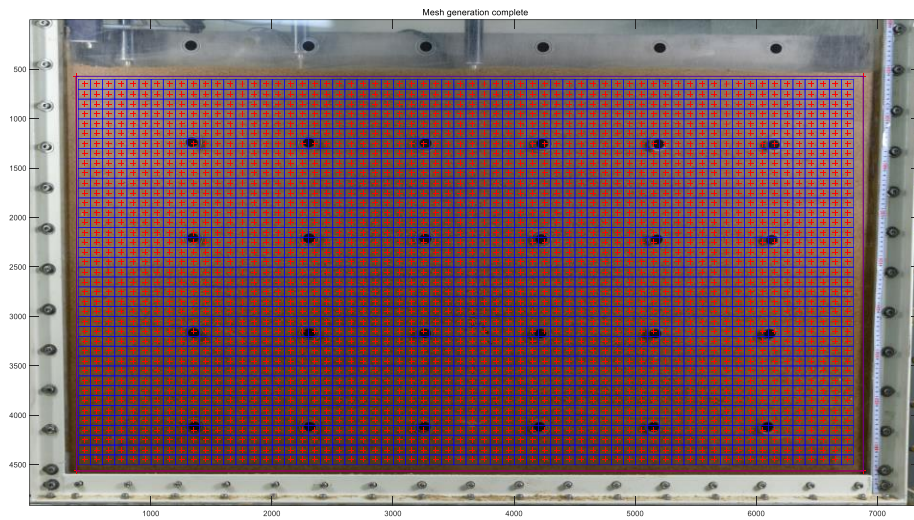
467

Figure 2: Grain distribution of the natural Gwanak soil and the Gwanak soil adjusted as per the requirements for backfill materials in South Korea (Ministry of Environment of Korea, 2010) and Japan (Japan Road Association, 1990).

468

469

470

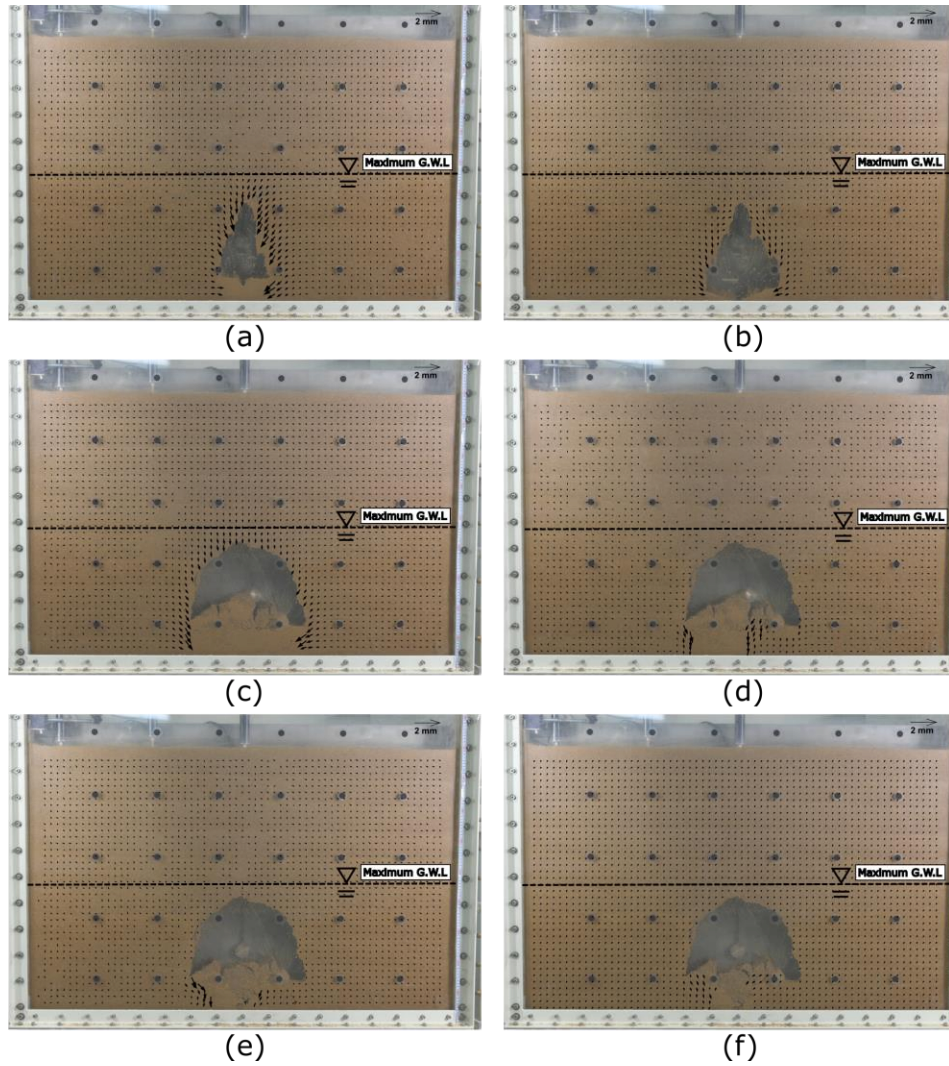


471

472

473

Figure 3: Selected pixel subsets and center points for digital image analysis.



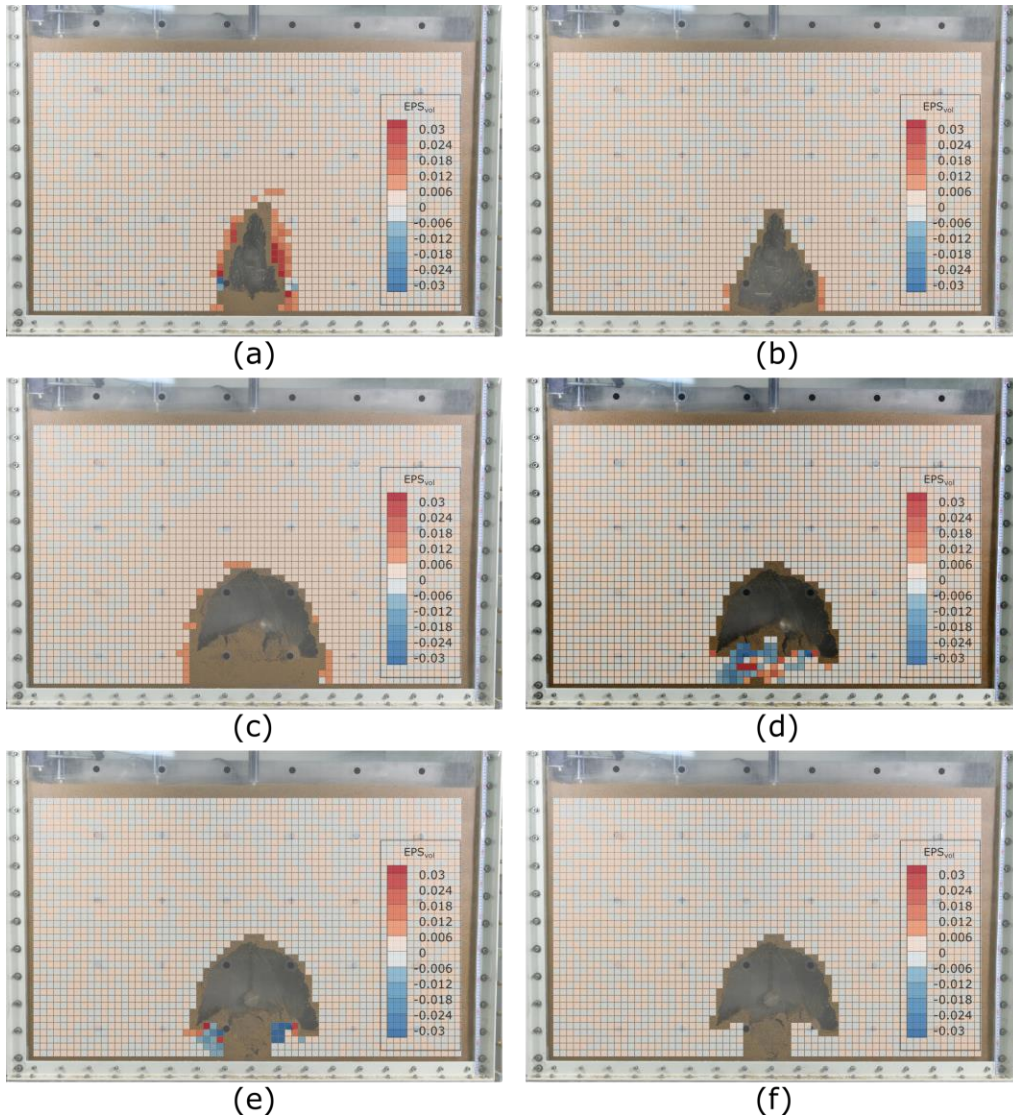
474

475

476

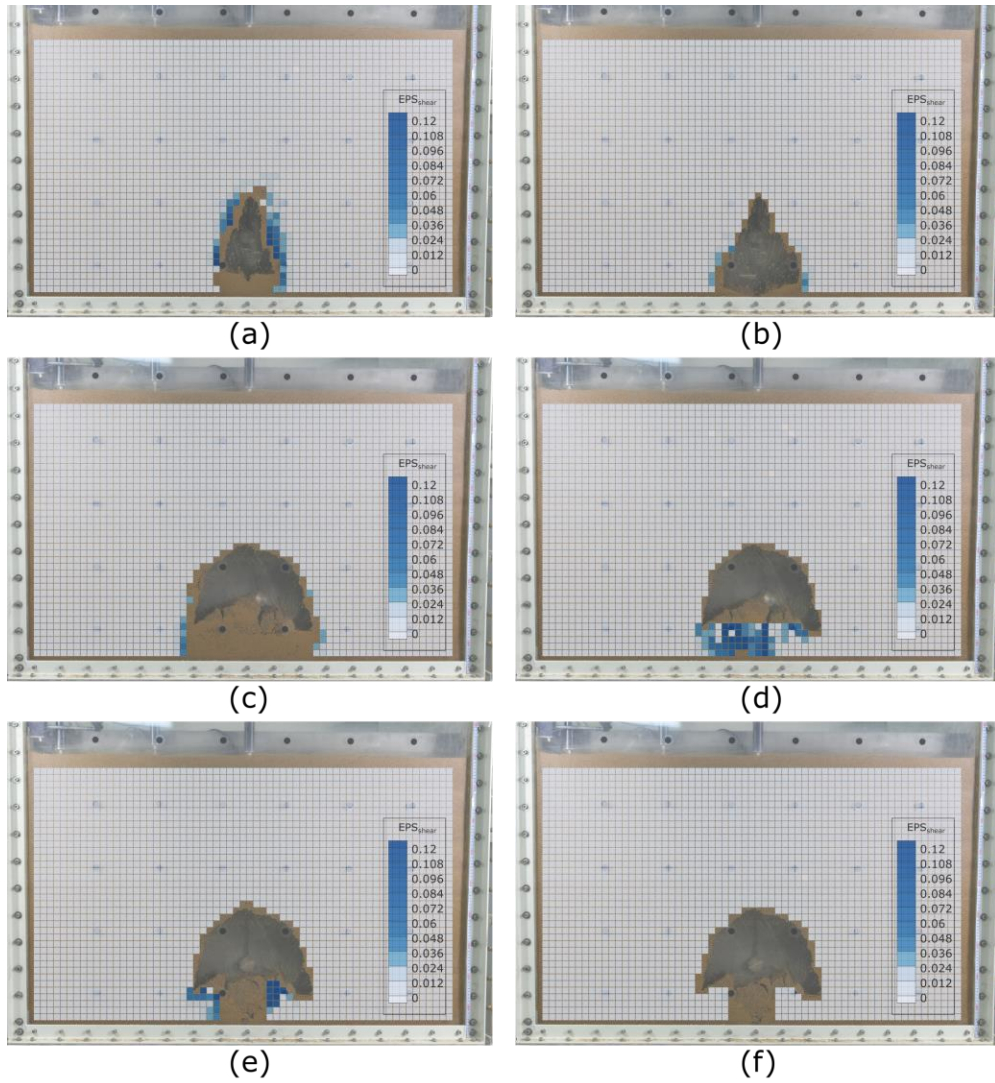
477

Figure 4: Displacement increment vectors inside the model ground for Test 1 during the water drainage stage: (a) 0–30 s, (b) 30–60 s, (c) 60–90 s, (d) 90–120 s, (e) 120–150 s, and (f) 150–180 s.



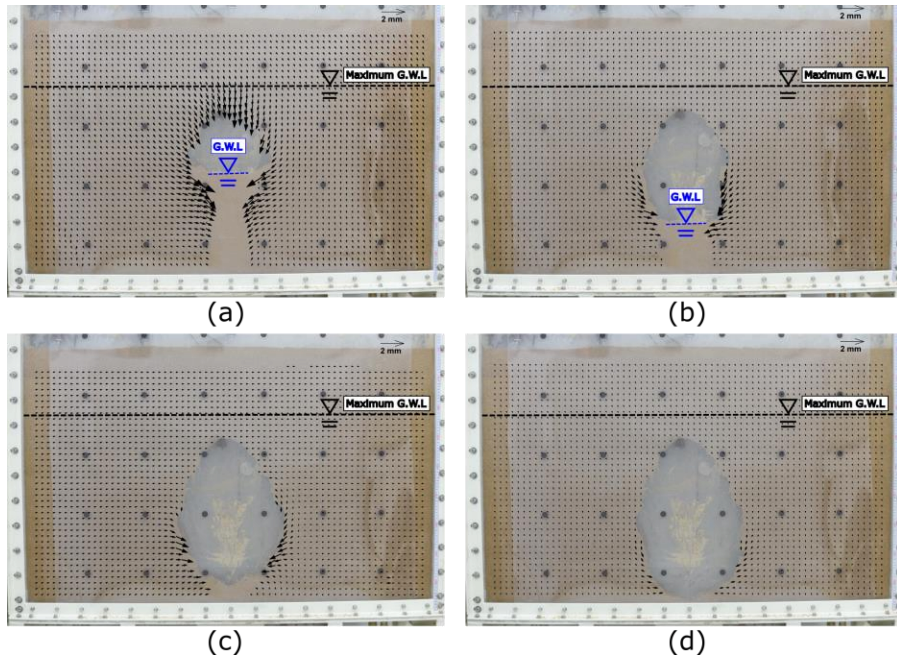
478
 479
 480
 481

Figure 5: Volumetric strain inside the model ground for Test 1 during the water drainage stage: (a) 0–30 s (b) 30–60 s, (c) 60–90 s, (d) 90–120 s, (e) 120–150 s, and (f) 150–180 s.



482
 483
 484
 485

Figure 6: Shear strain inside the model ground for Test 1 during the water drainage stage: (a) 0–30 s, (b) 30–60 s, (c) 60–90 s, (d) 90–120 s, (e) 120–150 s, and (f) 150–180 s.



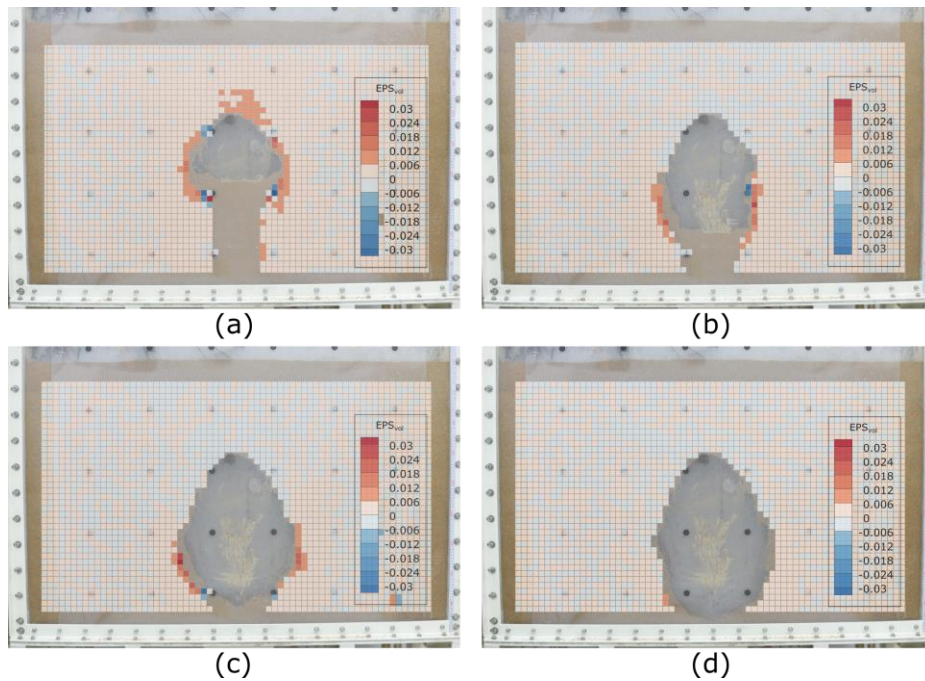
486

487

488

Figure 7: Displacement increment vectors inside the model ground for Test 2 during the water drainage stage: (a) 0–30 s, (b) 30–60 s, (c) 60–90 s, and (d) 90–120 s.

489



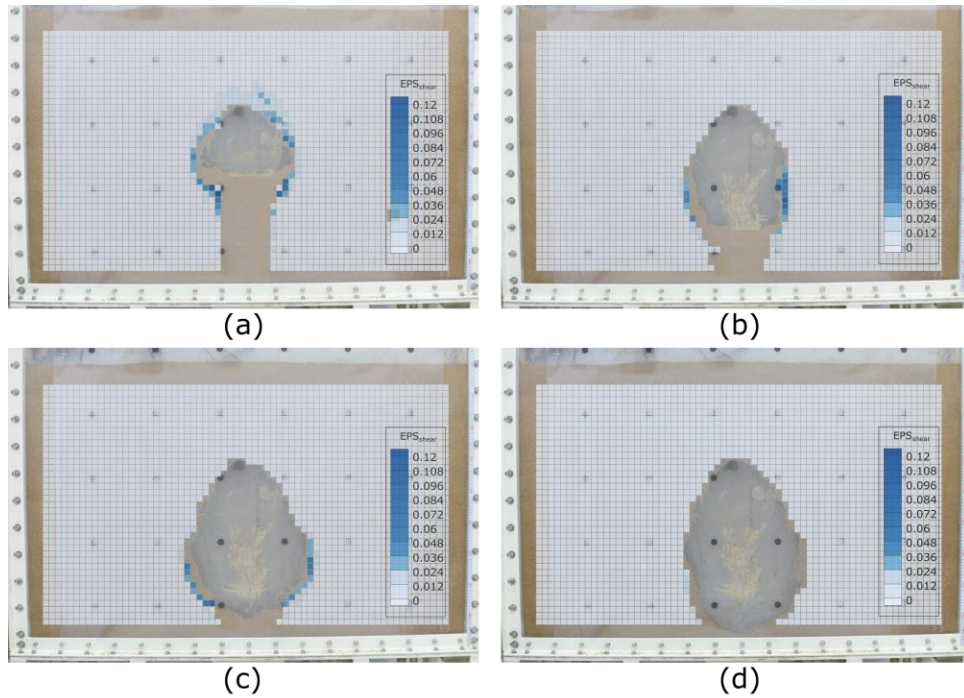
490

491

492

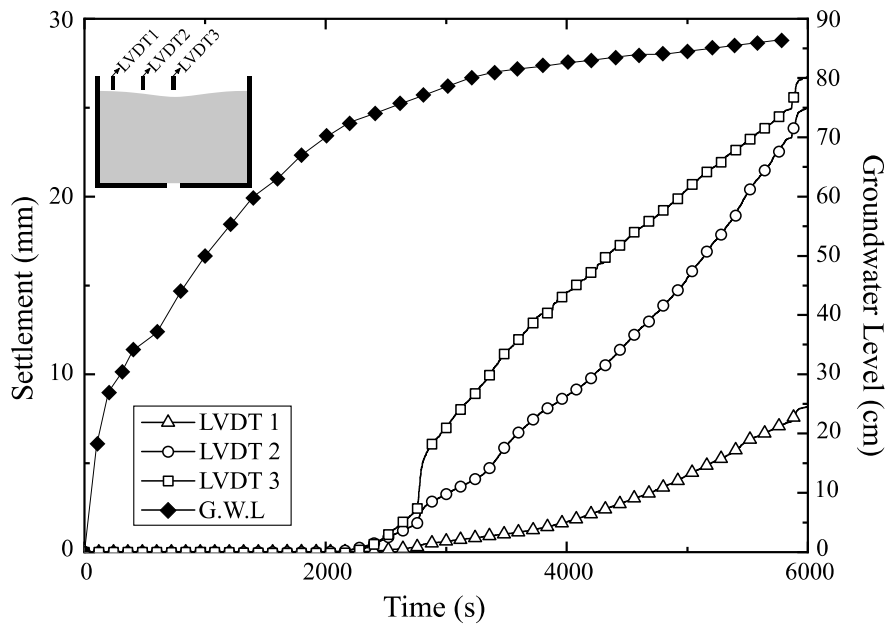
Figure 8: Volumetric strain inside the model ground for Test 2 during the water drainage stage: (a) 0–30 s, (b) 30–60 s, (c) 60–90 s, and (d) 90–120 s.

493



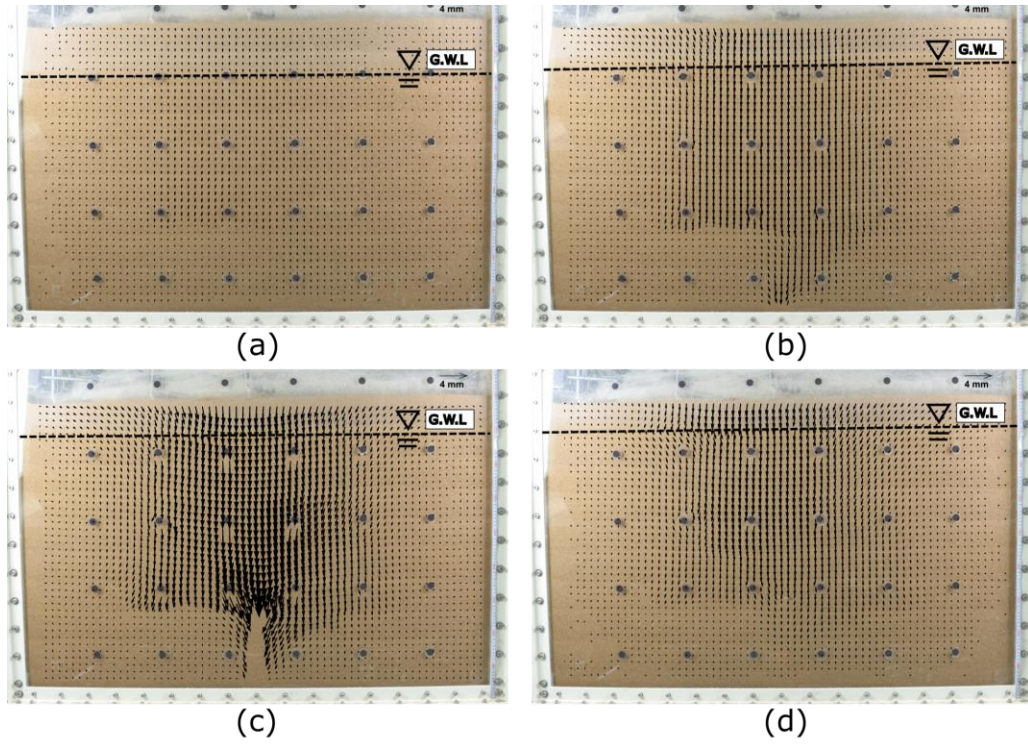
494
495
496
497

Figure 9: Shear strain inside the model ground for Test 2 during the water drainage stage: (a) 0–30 s, (b) 30–60 s, (c) 60–90 s, and (d) 90–120 s.



498
499
500

Figure 10: LVDT measurement during the water supply stage (Test 3).



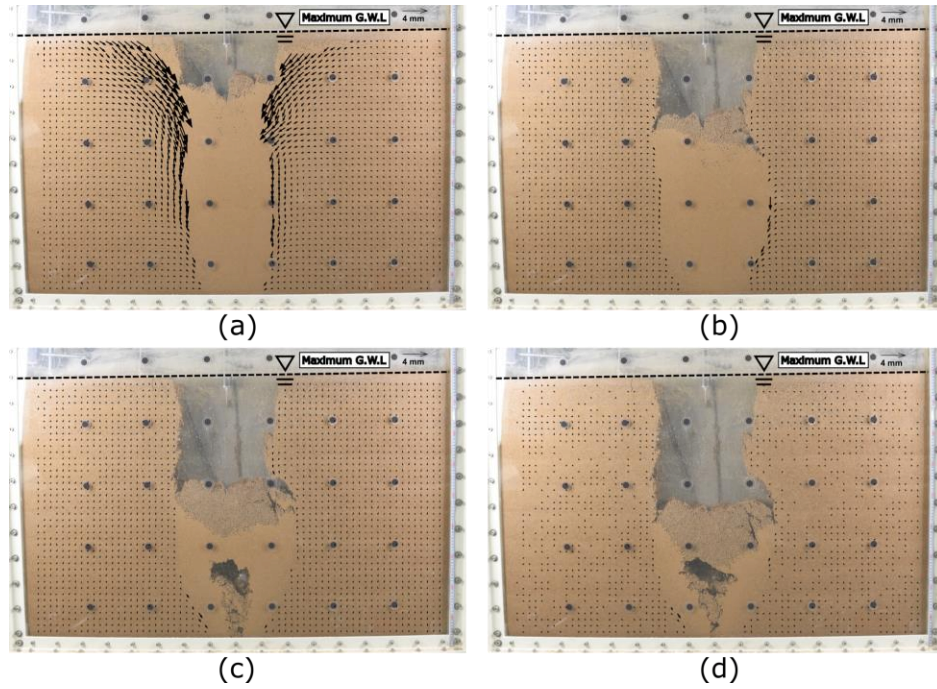
501

502

503

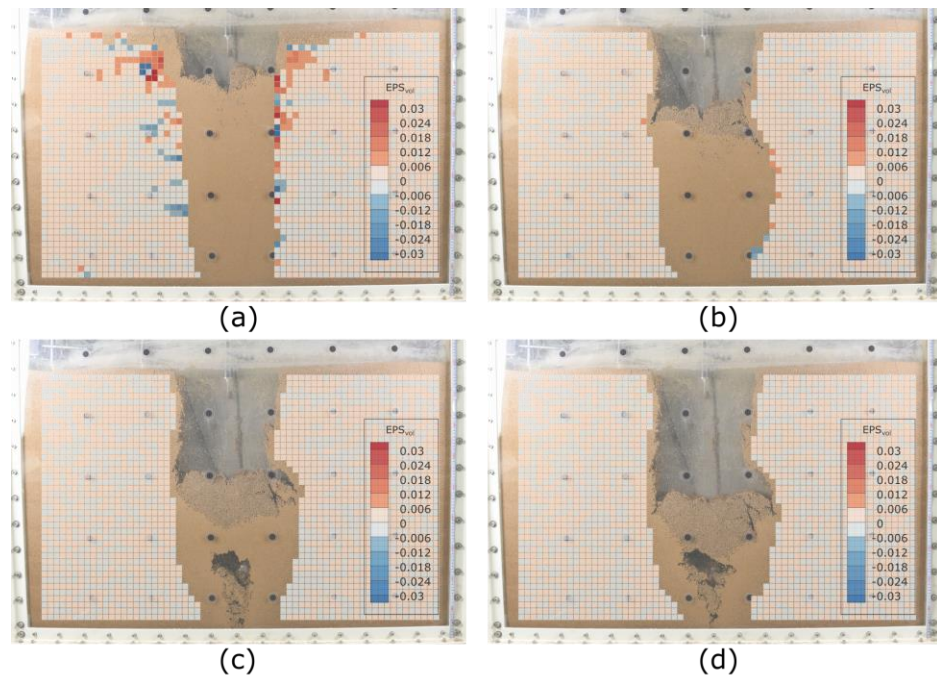
Figure 11: Displacement increment vectors inside the model ground for Test 3 during the water supply stage: (a) 2000–2400 s, (b) 2400–2800 s, (c) 2800–3200 s, and (d) 3200–3600 s.

504



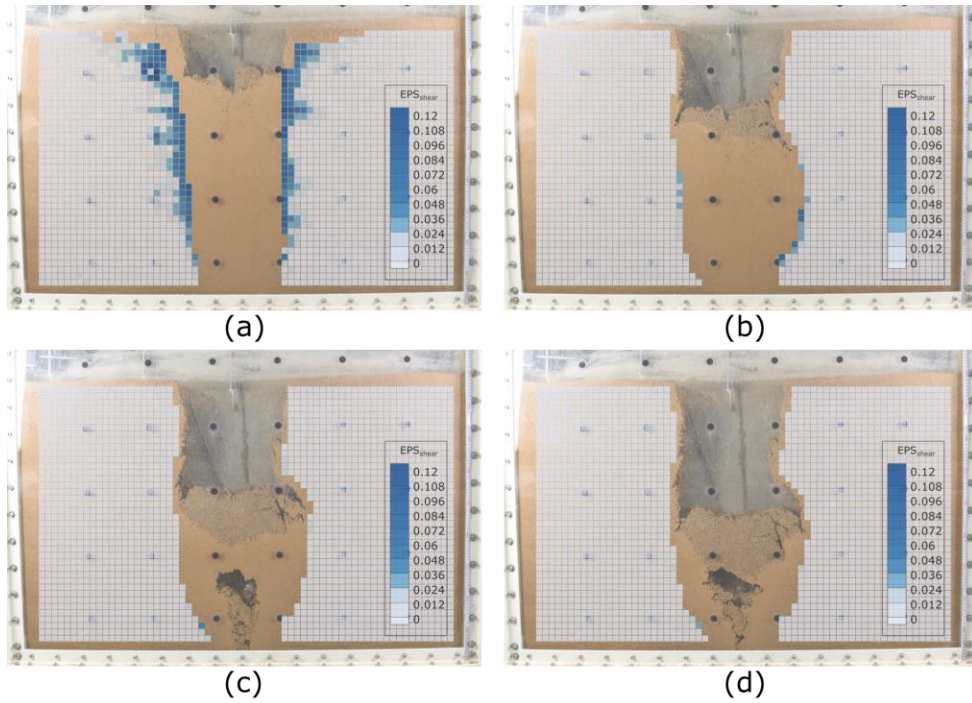
505
506
507

Figure 12: Displacement increment vectors inside the model ground for Test 3 during the water drainage stage: (a) 0–30 s, (b) 30–60 s, (c) 60–90 s, and (d) 90–120 s.



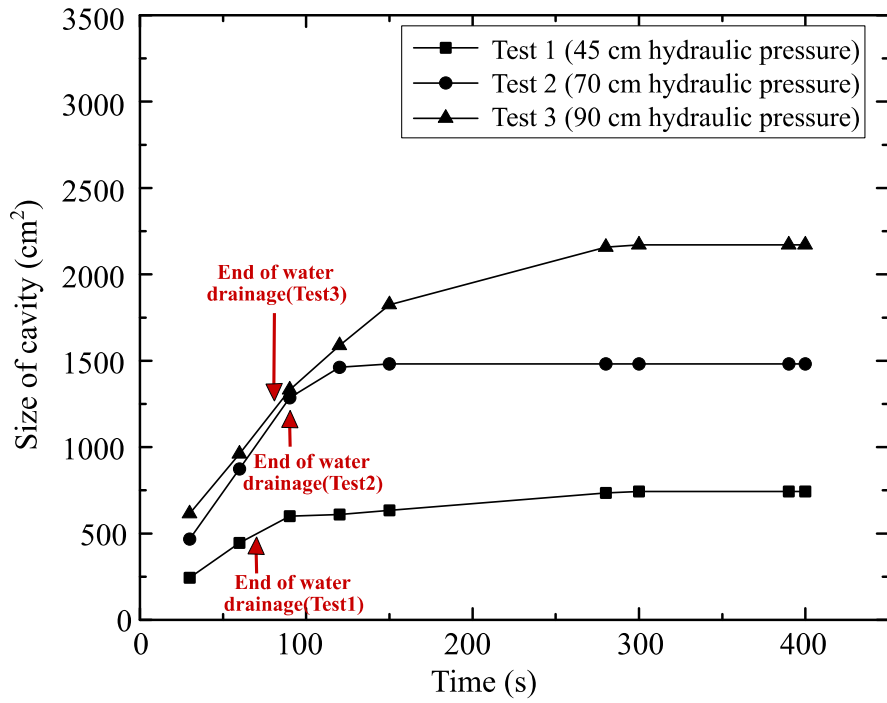
508
509
510
511

Figure 13: Volumetric strain inside the model ground for Test 3 during the water drainage stage: (a) 0–30 s, (b) 30–60 s, (c) 60–90 s, and (d) 90–120 s.



512
513
514
515

Figure 14: Shear strain inside the model ground for Test 3 during the water drainage stage: (a) 0–30 s, (b) 30–60 s, (c) 60–90 s, and (d) 90–120 s.



516
517

Figure 15: Sizes of cavities developed during the water drainage stage in each test.

518 **Table 1: Relation between rainfall intensity and hydraulic head applied to sewer pipes**
 519 **(National Disaster Management Institute of Korea, 2014).**

| Rainfall intensity | Hydraulic head |
|--------------------|----------------|
| 20 mm/h | 33 cm |
| 30 mm/h | 40 cm |
| 40 mm/h | 47 cm |
| 50 mm/h | 70 cm |

520

521 **Table 2: Properties of adjusted Gwanak soil.**

| Description | Adjusted Gwanak soil (Fine content 7.5 %) | | |
|---|--|---------------------------|------|
| Classification in USCS (Unified Soil Classification System) | SW-SM | | |
| Specific gravity G_s | 2.62 | | |
| Mean grain size D_{50} (mm) | 1.013 | | |
| Coefficient of curvature C_c | 1.24 | | |
| Coefficient of uniformity C_u | 12.4 | | |
| Standard maximum dry unit weight* $\gamma_{d,max}$ (kN/m ³) | 18.5 | | |
| e_{max} / e_{min} | 0.96 / 0.39 | | |
| Void ratio | 0.51 | | |
| Optimum water content* (%) | 11.4 | | |
| Strength parameter** | Saturation S 100 % | Cohesion c (kPa) | 3.9 |
| | | Friction angle ϕ (°) | 36.3 |
| | Saturation S 44.2 % | Cohesion c (kPa) | 15.8 |
| | | Friction angle ϕ (°) | 38.3 |
| Saturated permeability coefficient k_{sat} (cm/s) | 1.45 x 10 ⁻⁴ | | |

522 * Estimated from the standard compaction tests

523 ** Estimated from the direct shear tests; S = 44.2 % corresponds to w_{opt} obtained from the standard compaction tests

524 **Table 3: Model test conditions used in this study.**

| Test No. | Soil type | Slit size | Degree of compaction D_C (Relative density D_R) | Burial depth | Maximum groundwater level |
|----------|----------------------|-----------|---|--------------|---------------------------|
| #1 | Adjusted Gwanak soil | 2 cm | 93 % (78 %) | 90 cm | 47 cm |
| #2 | | | | | 70 cm |
| #3 | | | | | 90 cm |

525

526 **Table 4: Comparative studies of the model tests.**

| Test | Test 1 (47 cm G.W.L) | Test 2 (70 cm G.W.L) | Test 3 (90 cm G.W.L) |
|---|-------------------------|-------------------------|-------------------------|
| Percentage of the weight of the discharged soil in the total initial weight of the model ground | 6.4 % | 12.9 % | 18.3 % |
| Percentage of the volume of the eroded zone(cavity or ground cave-in) in the total initial volume of the model ground | 5.9 % | 12.5 % | 18.2 % |
| Ratio of average cavity width to slit width | 11.5 (22.9 / 2 cm) | 13.1 (26.2 / 2 cm) | 16.4 (32.8 / 2 cm) |
| Average density change in the loosening zone | -3.1 kN/m ³ | -3.7 kN/m ³ | -2.9 kN/m ³ |

527